

Photo-induced Floquet Weyl magnons in noncollinear antiferromagnets

S. A. Owerre¹

¹*Perimeter Institute for Theoretical Physics, 31 Caroline St. N., Waterloo, Ontario N2L 2Y5, Canada.*

We study periodically driven insulating noncollinear stacked kagome antiferromagnets with a conventional symmetry-protected three-dimensional (3D) in-plane 120° spin structure, with either positive or negative vector chirality. We show that the symmetry protection of the in-plane 120° spin structure can be broken in the presence of an off-resonant circularly or linearly polarized electric field propagating parallel to the in-plane 120° spin structure (say along the x direction). Consequently, topological Floquet Weyl magnon nodes with opposite chirality are photoinduced along the k_x momentum direction. They manifest as the monopoles of the photoinduced Berry curvature. We also show that the system exhibits a photoinduced magnon thermal Hall effect for circularly polarized electric field. Furthermore, we show that the photoinduced chiral spin structure is a canted 3D in-plane 120° spin structure, which was recently observed in the equilibrium noncollinear antiferromagnetic Weyl semimetals Mn₃Sn/Ge. Our result not only paves the way towards the experimental realization of Weyl magnons and photoinduced thermal Hall effects, but also provides a powerful mechanism for manipulating the intrinsic properties of 3D topological antiferromagnets.

I. INTRODUCTION

In recent years, the Floquet engineering of topologically nontrivial systems from topologically trivial ones has attracted considerable attention in electronic systems [1–23]. However, its application to realistic three-dimensional (3D) materials is very limited. To our knowledge, a photoinduced Floquet Weyl semimetal has only been created in the non-magnetic 3D Dirac semimetal Na₃Bi [18]. In the electronic Floquet topological systems, the intensity of light is characterized by a dimensionless quantity given by [1–5]

$$\mathcal{E}_i = \frac{eE_i a}{\hbar\omega}, \quad (1)$$

where E_i ($i = x, y, z$) are the amplitudes of the electric field, e is the electron charge, ω is the angular frequency of light, a is the lattice constant, and \hbar is the reduced Planck's constant. In the magnetic bosonic Floquet topological systems, however, the intensity of light is characterized by a dimensionless quantity given by [24]

$$\mathcal{E}_i = \frac{g\mu_B E_i a}{\hbar c^2}, \quad (2)$$

where g is the Landé g -factor, μ_B is the Bohr magneton, and c is the speed of light. The lack of frequency dependence in Eq. (2) unlike in Eq. (1) is because it originates from the Aharonov-Casher phase [25], which is a topological phase acquires by a neutral particle with magnetic dipole moment (such as magnon) in the presence of an electric field. By equating the two dimensionless quantities we can see that the spin magnetic dipole moment $g\mu_B$ carried by magnon in the periodically driven insulating magnets is given by

$$g\mu_B = \frac{ec^2}{\omega} = \frac{ec\lambda}{2\pi}. \quad (3)$$

Therefore for an experimentally feasible light wavelength λ of order 10^{-8} m, the spin magnetic dipole moment $g\mu_B$ carried by magnon in the periodically driven insulating magnets is comparable to the electron charge e . This shows that the electronic Floquet topological systems [1–5] are indeed similar to the magnetic bosonic Floquet topological systems recently studied in insulating ferromagnets with finite magnetization [24, 26–28]. In magnetic systems, however, the Floquet physics can reshape the underlying spin Hamiltonian to stabilize magnetic phases and provides a promising avenue for inducing and tuning topological spin excitations in trivial quantum magnets [24, 26, 27], as well as photoinduced topological phase transitions in intrinsic topological magnon insulators [28]. This formalism provides a direct avenue of generating and manipulating ultrafast spin current using terahertz radiation [29].

Interesting features are expected to manifest in periodically driven insulating antiferromagnets with zero net magnetization. Recently, the equilibrium topological aspects of 3D insulating antiferromagnets including Weyl magnons and topological thermal Hall effects have attracted considerable attention [30–37]. They can be induced from 3D noncollinear spin structure by applying an external magnetic field or including an in-plane Dzyaloshinskii-Moriya interaction (DM) interaction [38, 39]. For the stacked kagome antiferromagnets, the equilibrium Weyl magnon nodes are acoustic and they result from a noncoplanar spin structure with a nonzero scalar spin chirality, which breaks time-reversal symmetry macroscopically [32]. The question that remains is whether there is an alternative source to induce Weyl magnons and thermal Hall effect in 3D insulating noncollinear antiferromagnets.

In this paper, we provide an alternative avenue to induce acoustic Weyl magnon nodes and magnon thermal Hall effect in 3D noncollinear kagome antiferromagnets. We study periodically driven symmetry-protected 3D in-plane 120° spin structure with either positive or negative

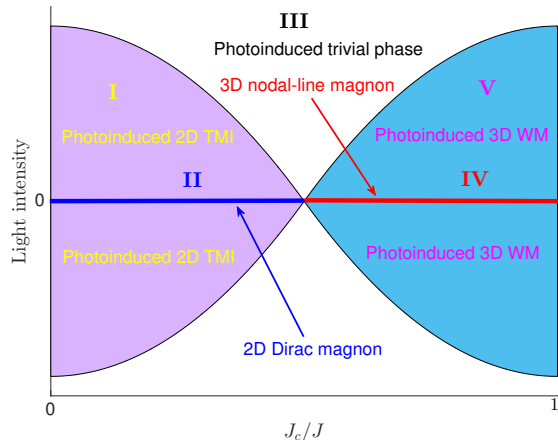


FIG. 1. Color online. Schematic of the topological phase diagram in periodically driven noncollinear kagome antiferromagnets as a function of the light intensity and the antiferromagnetic interlayer coupling. There are five identified phases. For negligible antiferromagnetic interlayer coupling $J_c/J \ll 1$ there are two phases labeled as *I* and *II* corresponding to photoinduced 2D topological magnon insulator (TMI) and undriven 2D Dirac magnon at zero oscillating electric field respectively. For non-negligible antiferromagnetic interlayer coupling $0 < J_c/J \leq 1$ there are three phases labeled as *III*, *IV*, and *V* corresponding to photoinduced 3D trivial magnon insulator, undriven 3D nodal line magnon at zero oscillating electric field, and photoinduced 3D Weyl magnon (WM) respectively.

vector chirality in the stacked kagome-lattice antiferromagnets. The photoinduced topological phase diagram of the model is schematically shown in Fig. (1). In the main paper, we consider regions *IV* and *V* when the antiferromagnetic interlayer coupling is not negligible. The 2D phases for negligible interlayer coupling will be studied in the appendix. The 3D nodal line magnons and triply-degenerate nodal magnon points are present at zero light intensity in the in-plane 120° spin structure. They are protected by crystal and time-reversal symmetries of the kagome lattice [32]. As the periodic drive is turned on parallel to the in-plane 120° spin structure, we show that its symmetry protection is broken by the laser field.

As a result, we obtain non-degenerate magnon quasienergy linear band crossings, which form topological Floquet Weyl magnon nodes with opposite chirality along the k_x direction on the $k_z = \pi$ plane. The photoinduced topological Floquet Weyl magnon nodes are present for both linearly- and circularly-polarized light. However, we show that the photoinduced thermal Hall effect which characterizes a measurable topological magnon transport property of the system is only present for circularly-polarized light. This means that the thermal Hall transport for linearly-polarized light is topologically trivial. We also show that the photoinduced chiral spin structure is the canted 3D in-plane 120° spin structure in analogy to the chiral spin structure recently observed in the non-

collinear antiferromagnetic Weyl semimetals $\text{Mn}_3\text{Sn}/\text{Ge}$ [48–51]. Therefore, the current results are different from the equilibrium Weyl magnons induced by noncoplanar spin structure with a nonzero scalar spin chirality [32]. Our results provide a powerful mechanism for manipulating the intrinsic properties of insulating geometrically frustrated kagome antiferromagnets such as jarosites [40], herbertsmithite [41], and Cd-kapellasite [42].

II. TIME-INDEPENDENT NONCOLLINEAR KAGOMÉ ANTIFERROMAGNETS

A. Heisenberg spin model

We study stacked frustrated kagomé antiferromagnets governed by the microscopic Heisenberg spin Hamiltonian

$$\mathcal{H} = J \sum_{\langle ij \rangle, \ell} \vec{S}_{i, \ell} \cdot \vec{S}_{j, \ell} + \sum_{\langle ij \rangle, \ell} \vec{D}_{ij} \cdot \vec{S}_{i, \ell} \times \vec{S}_{j, \ell} + J_c \sum_{i, (\ell \ell')} \vec{S}_{i, \ell} \cdot \vec{S}_{i, \ell'}, \quad (4)$$

where i and j denote the sites on the kagomé layers, ℓ and ℓ' label the layers. The first term corresponds to the nearest-neighbour (NN) antiferromagnetic intralayer Heisenberg interaction. The second term is the out-of-plane ($\vec{D}_{ij} = \pm D_z \hat{z}$) DM interaction due to lack of inversion symmetry between two sites on each kagomé layer. The DM interaction alternates between the triangular plaquettes of the kagomé lattice as shown in Figs. (2)(a) and (b). It also stabilizes the conventional 3D in-plane 120° non-collinear spin structure. Its sign determines the vector chirality of the non-collinear spin order [43]. The third term is the NN interlayer antiferromagnetic Heisenberg interaction between the kagomé layers.

B. Symmetry protection of the conventional in-plane 120° spin structure

As explicitly discussed in ref. [32], the conventional 3D in-plane 120° spin structure preserves all the symmetries of the kagomé lattice. In particular, the combination of time-reversal symmetry (denoted by \mathcal{T}) and spin rotation denoted by $\mathcal{R}_z(\pi)$ is a good symmetry, where $\mathcal{R}_z(\pi) = \text{diag}(-1, -1, 1)$ denotes a π spin rotation of the in-plane coplanar spins about the z -axis, and ‘diag’ denotes diagonal elements. In addition, the system also has three-fold rotation symmetry along the z direction denoted by \mathcal{C}_3 . The combination of mirror reflection symmetry of the kagome plane about the x or y axis and \mathcal{T} (*i.e.* $\mathcal{T}\mathcal{M}_x\mathcal{T}$ or $\mathcal{M}_y\mathcal{T}$) is also a symmetry of the conventional in-plane 120° non-collinear spin structure. These symmetries are known as the “effective time-reversal symmetry” [44, 45], and they lead to protection of nodal-line magnons and triply-degenerate nodal magnon points in

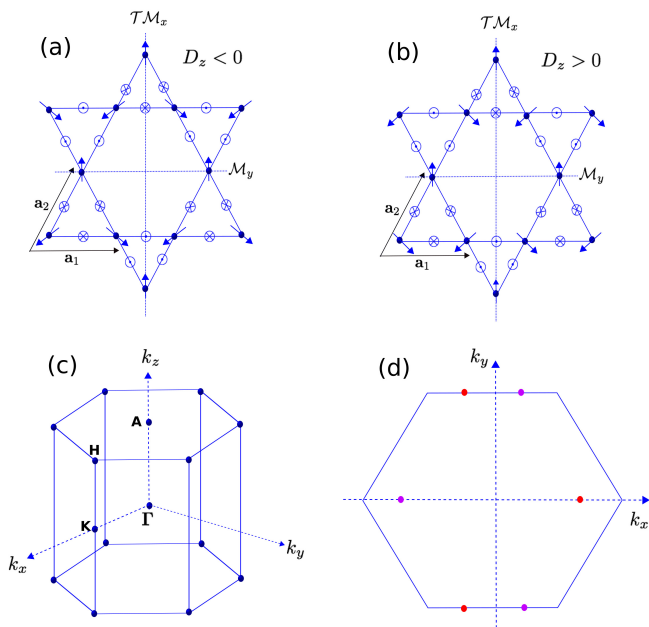


FIG. 2. Color online. Top panel. Top view of congruently stacked noncollinear kagome antiferromagnets along the (001) direction. The conventional in-plane 120° non-collinear spin configuration is indicated by the blue arrows. The in-plane unit vectors are $\mathbf{a}_1 = (1, 0, 0)$ and $\mathbf{a}_2 = (1/2, \sqrt{3}/2, 0)$. The unit vector along the stacking direction $\mathbf{a}_z = (0, 0, 1)$ is not depicted. The mirror reflection axes (dotted lines) and the direction of the alternating DM interaction (crossed and dotted circles) are indicated. (a) Positive vector chirality for $D_z < 0$. (b) Negative vector chirality for $D_z > 0$. Bottom panel. The Brillouin zone (BZ) of the hexagonal lattice. (c) The bulk BZ with indicated high-symmetry points. (d). The (001) surface BZ with 3 pairs of Floquet Weyl points with opposite chiralities (red and pink dots) along the k_x direction.

the conventional 3D in-plane 120° spin structure of the stacked kagome antiferromagnets. The goal of this paper is to periodically drive these trivial magnon phases to a topological Floquet Weyl magnon phase without the effects of an external magnetic field or an in-plane DM interaction.

III. TIME-DEPENDENT NONCOLLINEAR KAGOMÉ ANTIFERROMAGNETS

In this section, we will study regions *IV* and *V* in Fig. (1).

A. Theoretical formulation

The concept of periodically driven magnetic insulators rely on the spin magnetic dipole moments carried by the underlying magnon excitations as previously introduced in quantum ferromagnets [24, 26, 28]. In other words, charge-neutral bosonic quasiparticles can interact

with an electromagnetic field through their spin magnetic dipole moment. The corresponding time-dependent version of the Aharonov-Casher phase [25] emerges explicitly from quantum field theory with the Dirac-Pauli Lagrangian [26, 28]. We take the spin magnetic dipole moment carried by magnons to be along the in-plane ordering direction $\vec{\mu} = g\mu_B\hat{x}$. In the presence of an oscillating electric field $\vec{E}(\tau)$ propagating along the in-plane x direction, magnons accumulate the time-dependent version of the Aharonov-Casher phase, given by

$$\Phi_{ij}(\tau) = \mu_m \int_{\vec{r}_i}^{\vec{r}_j} \vec{\Xi}(\tau) \cdot d\vec{\ell}, \quad (5)$$

where $\mu_m = g\mu_B/\hbar c^2$. We have used the notation $\vec{\Xi}(\tau) = \vec{E}(\tau) \times \hat{x}$ for brevity, where $\vec{E}(\tau) = -\partial_\tau \vec{A}(\tau)$ and $\vec{A}(\tau)$ is the time-periodic vector potential. It is important to note that the magnon accumulated time-dependent version of the Aharonov-Casher phase in Eq. (5) is different from that of static time-independent electric field [46, 47] for which the relations in Eqs. (2) and (3) do not apply. For light propagating along the in-plane x direction perpendicular to the $y-z$ plane, we choose the time-periodic vector potential such that

$$\vec{\Xi}(\tau) = [0, E_y \sin(\omega\tau), E_z \sin(\omega\tau + \phi)], \quad (6)$$

where ϕ is the phase difference. Circularly-polarized electric field corresponds to $\phi = \pi/2$, whereas linearly-polarized electric field corresponds to $\phi = 0$ or π .

B. Effective spin Hamiltonian

In the absence of an in-plane DM interaction and an external magnetic field, the positive and negative vector chiralities in Figs. (2)(a) and (b) essentially yield the same magnon dispersions, when an appropriate spin rotation is performed. In fact, both spin configurations in Figs. (2)(a) and (b) are related by two-fold rotation about the y -axis. Therefore, we will restrict our study to the positive vector chirality, and rotate the coordinate axis about the z -axis by the spin orientation angles $\theta_{i,\ell}$

$$S_{i,\ell}^x = \cos \theta_{i,\ell} S_{i,\ell}'^x - \sin \theta_{i,\ell} S_{i,\ell}'^y, \quad (7)$$

$$S_{i,\ell}^y = \sin \theta_{i,\ell} S_{i,\ell}'^x + \cos \theta_{i,\ell} S_{i,\ell}'^y, \quad (8)$$

$$S_{i,\ell}^z = S_{i,\ell}'^z, \quad (9)$$

where $\theta_{i,\ell} = 0, 2\pi/3, -2\pi/3$ for spins on sublattice A, B, C respectively as denoted in Fig. (2)(a). The prime denotes the rotated coordinate. We choose the spin quantization axis along the x -axis such that $S_{i,\ell}^\pm = S_{i,\ell}'^y \pm iS_{i,\ell}'^z$ are the raising and lowering operators.

After substituting the spin transformation into Eq. (4), the time-dependent phase in Eq. (5) couples to the spin Hamiltonian through the off-diagonal terms such as $(S_{i,\ell}'^+ S_{j,\ell}'^- e^{i\Phi_{ij,\ell}(\tau)} + \text{H.c.})$ and $(S_{i,\ell}'^+ S_{j,\ell}'^+ e^{i\Phi_{ij,\ell}(\tau)} + \text{H.c.})$

for the intralayer in-plane spin interactions, as well as ($S_{i,\ell}^+ S_{i,\ell'}^- e^{i\Phi_{i,\ell\ell'}(\tau)} + \text{H.c.}$) and ($S_{i,\ell}^+ S_{i,\ell'}^+ e^{i\Phi_{i,\ell\ell'}(\tau)} + \text{H.c.}$) for the interlayer spin interaction. In the off-resonant limit when the photon energy $\hbar\omega$ is greater than the energy scale of the undriven system, the effective static Hamiltonian is given by [5] $\mathcal{H}_{eff} \approx \mathcal{H}_0 + \Delta\mathcal{H}_{eff}$, where $\Delta\mathcal{H}_{eff} = [\mathcal{H}_1, \mathcal{H}_{-1}]/\hbar\omega$ is the photon emission and absorption term and $\mathcal{H}_n = \frac{1}{T} \int_0^T d\tau e^{-in\omega\tau} \mathcal{H}(\tau)$ is the multi-photon Fourier components with period $T = 2\pi/\omega$. The first term \mathcal{H}_0 is the original static spin Hamiltonian with renormalized spin interactions, whereas the second term $\Delta\mathcal{H}_{eff}$ breaks time-reversal symmetry by inducing additional spin interactions via photon absorption and emission process. For simple spin model such as the Heisenberg ferromagnet the effective spin Hamiltonian can be derived explicitly [24]. An alternative approach to magnetic Floquet physics is to consider the charge degree of freedom through the Peierls phase in the Hubbard model, which also maps to a renormalized effective spin model in the off-resonant limit [22, 23]. This approach, how-

ever, does not explicitly show how the spins couple to the laser electric field in insulating magnets with charge neutral excitation. Due to the complexity of the present model, the explicit derivation of the effective spin Hamiltonian in the off-resonant limit is very cumbersome.

C. Bosonic Bogoliubov-de Gennes Hamiltonian

Our main objective is to study the effects of light on the magnon band structure of 3D non-collinear antiferromagnets. Hence, it is advantageous to use linear spin wave theory via the implementation of the linearized Holstein-Primakoff transformation

$$S_{i,\ell}^{\prime x} = S - a_{i,\ell}^\dagger a_{i,\ell}, \quad S_{i,\ell}^{\prime +} \approx \sqrt{2S} a_{i,\ell} = (S_{i,\ell}^{\prime -})^\dagger, \quad (10)$$

where $a_{i,\ell}^\dagger$ ($a_{i,\ell}$) are the bosonic creation (annihilation) operators. By substituting the Holstein-Primakoff transformation directly into the resulting time-dependent spin Hamiltonian $\mathcal{H}(\tau)$, the corresponding time-dependent linear spin-wave Hamiltonian is given by

$$\begin{aligned} \mathcal{H}(\tau) = & JS \sum_{\langle ij \rangle, \ell} \left[t_0 (a_{i,\ell}^\dagger a_{i,\ell} + a_{j,\ell}^\dagger a_{j,\ell}) + t_1 (a_{i,\ell}^\dagger a_{j,\ell} e^{i\Phi_{ij,\ell}(\tau)} + \text{H.c.}) + t_2 (a_{i,\ell}^\dagger a_{j,\ell}^\dagger e^{i\Phi_{ij,\ell}(\tau)} + \text{H.c.}) \right] \\ & + J_c S \sum_{i, \langle \ell\ell' \rangle} \left[(a_{i,\ell}^\dagger a_{i,\ell} + a_{i,\ell'}^\dagger a_{i,\ell'}) + (a_{i,\ell}^\dagger a_{i,\ell'}^\dagger e^{i\Phi_{i,\ell\ell'}(\tau)} + \text{H.c.}) \right], \end{aligned} \quad (11)$$

where $t_0 = (1 + \sqrt{3}D_z/J)/2$; $t_1 = (1 - \sqrt{3}D_z/J)/4$; $t_2 = (3 + \sqrt{3}D_z/J)/4$. The hopping terms acquire a time-dependent phase factor by virtue of the Peierls substitution as discussed above. The corresponding time-dependent bosonic Bogoliubov-de Gennes (BdG) Hamiltonian is given by

$$\mathcal{H}(\tau) = \frac{1}{2} \sum_{\vec{k}} (u^\dagger(\vec{k}), u(-\vec{k})) \cdot \mathcal{H}(\vec{k}, \tau) \cdot \begin{pmatrix} u(\vec{k}) \\ u^\dagger(-\vec{k}) \end{pmatrix}, \quad (12)$$

where $u^\dagger(\vec{k}) = (a_{\vec{k}A}^\dagger, a_{\vec{k}B}^\dagger, a_{\vec{k}C}^\dagger)$ is the basis vector.

$$\mathcal{H}(\vec{k}, \tau) = 2JS \begin{pmatrix} \mathcal{G}^d(\vec{k}, \tau) & \mathcal{G}^o(\vec{k}, \tau) \\ \mathcal{G}^o(\vec{k}, \tau) & \mathcal{G}^d(\vec{k}, \tau) \end{pmatrix}. \quad (13)$$

The 3×3 matrices are given by

$$\mathcal{G}^d(\vec{k}, \tau) = \Lambda^0 + t_1 \Lambda(\vec{k}_\parallel, \tau), \quad (14)$$

$$\mathcal{G}^o(\vec{k}, \tau) = t_2 \Lambda(\vec{k}_\parallel, \tau) + t_c \Lambda^z(k_z, \tau), \quad (15)$$

where $t_c = J_c/J$. The Λ matrices are given by

$$\Lambda^0 = (2t_0 + t_c) \mathbf{I}_{3 \times 3}, \quad \Lambda^z(k_z, \tau) = \cos k_z(\tau) \mathbf{I}_{3 \times 3}, \quad (16)$$

$$\Lambda(\vec{k}_\parallel, \tau) = \begin{pmatrix} 0 & \gamma_{AB}(k_\parallel, \tau) & \gamma_{CA}(k_\parallel, \tau) \\ \gamma_{AB}^*(k_\parallel, \tau) & 0 & \gamma_{BC}(k_\parallel, \tau) \\ \gamma_{CA}^*(k_\parallel, \tau) & \gamma_{BC}^*(k_\parallel, \tau) & 0 \end{pmatrix}, \quad (17)$$

where

$$\gamma_{AB}(k_\parallel, \tau) = \cos k_1^\parallel(\tau), \quad (18)$$

$$\gamma_{BC}(k_\parallel, \tau) = \cos k_2^\parallel(\tau), \quad (19)$$

$$\gamma_{CA}(k_\parallel, \tau) = \cos k_3^\parallel(\tau), \quad (20)$$

with $k_i(\tau) = k_i + \mu_m \Xi(\tau)$ and $k_i^\parallel = \vec{k} \cdot \vec{a}_i$, with $\vec{a}_1 = a(\hat{x}/2 + \sqrt{3}\hat{y}/2)$, $\vec{a}_2 = a\hat{x}$, and $\vec{a}_3 = \vec{a}_1 - \vec{a}_2$.

D. Bosonic Floquet-Bloch theory

The Floquet theory is a powerful mechanism to study periodically driven quantum systems. In this formalism we can transform the time-dependent bosonic BdG Hamiltonian $\mathcal{H}(\vec{k}, \tau)$ into a static effective Hamiltonian governed by the Floquet bosonic BdG Hamiltonian. To do this we expand the time-dependent bosonic BdG

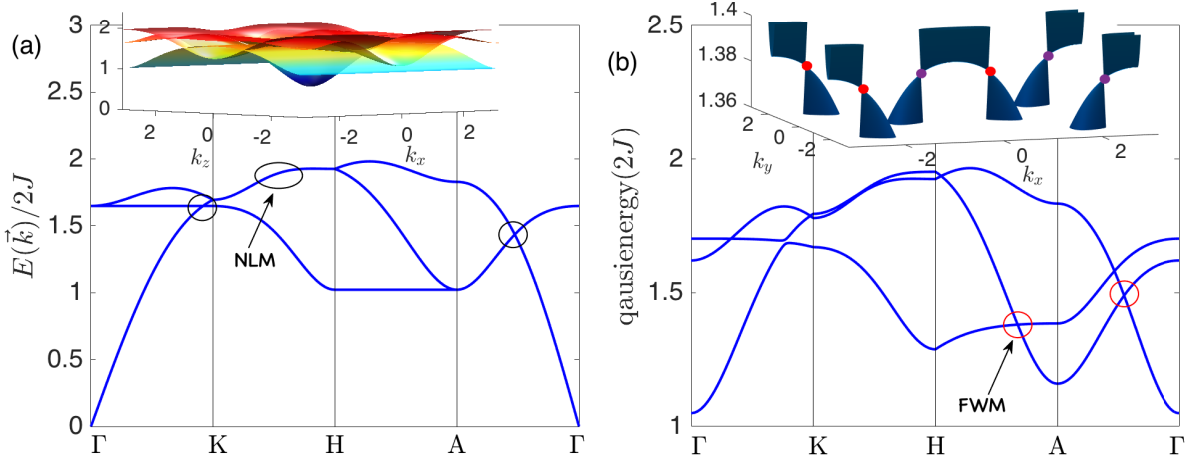


FIG. 3. Color online. (a) The magnon band structures of undriven 3D noncollinear kagome antiferromagnet showing a coexistence of 3D nodal-line magnons and triply-degenerate nodal magnon points for $S = 1/2$, $D_z/J = 0.2$, $J_c/J = 0.5$, $\mathcal{E}_y = \mathcal{E}_z = 0$. The black circles denote the nodal-line magnon (NLM) nodes. The magnon band crossing along $A-\Gamma$ line form triply-degenerate nodal magnon points. Inset shows the 3D magnon bands on the $k_y = 0$ plane. (b) The magnon quasienergy bands in the periodically driven 3D noncollinear kagome antiferromagnet for $S = 1/2$, $D_z/J = 0.2$, $J_c/J = 0.5$, $\mathcal{E}_y = \mathcal{E}_z = 1$, $\phi = \pi/2$ or $\phi = 0$, and $\omega/J = 10$. The red circles denote the photoinduced Floquet Weyl magnon (FWM) nodes at the acoustic branch. Inset shows the 3D topological Floquet Weyl magnon nodes on the $k_z = \pi$ plane. There are 3 pairs of Floquet Weyl magnon nodes with opposite chiralities on the $k_z = \pi$ plane located at $\vec{k}_{Q_1} = [\pm \cos^{-1}(Q_1), 0, \pi]$ and $\vec{k}_{Q_2} = [\pm \cos^{-1}(Q_2), \pm\pi/3, \pi]$. In addition, please note that the incident light breaks $U(1)$ spin rotation and lifts the Goldstone modes at the Γ point.

Hamiltonian as

$$\mathcal{H}(\vec{k}, \tau) = \sum_{n=-\infty}^{\infty} e^{in\omega\tau} \mathcal{H}_n(\vec{k}), \quad (21)$$

where $\mathcal{H}_n(\vec{k}) = \frac{1}{T} \int_0^T e^{-in\omega\tau} \mathcal{H}(\vec{k}, \tau) d\tau = \mathcal{H}_{-n}^\dagger(\vec{k})$ are the Fourier components. The corresponding eigenvectors can be written as $|\psi_{n'}(\vec{k}, \tau)\rangle = e^{-i\epsilon_{n'}(\vec{k})\tau} |\chi_{n'}(\vec{k}, \tau)\rangle$, where $|\chi_{n'}(\vec{k}, \tau)\rangle = |\chi_{n'}(\vec{k}, \tau + T)\rangle = \sum_n e^{in\omega\tau} |\chi_{n'}^n(\vec{k})\rangle$ is the time-periodic Floquet-Bloch wave function of magnons and $\epsilon_{n'}(\vec{k})$ are the magnon quasienergy bands. We define the Floquet operator as $\mathcal{H}^F(\vec{k}, \tau) = \mathcal{H}(\vec{k}, \tau) - i\partial_\tau$. The corresponding eigenvalue equation is of the form

$$\sum_m [\mathcal{H}_{n-m}(\vec{k}) + m\omega\delta_{n,m}] \chi_{n'}^m(\vec{k}) = \epsilon_{n'}(\vec{k}) \chi_{n'}^n(\vec{k}). \quad (22)$$

The Fourier components of the Floquet bosonic BdG Hamiltonian are given by

$$\mathcal{H}_q(\vec{k}) = 2JS \begin{pmatrix} \mathcal{G}_q^d(\vec{k}) & \mathcal{G}_q^o(\vec{k}) \\ \mathcal{G}_q^o(\vec{k}) & \mathcal{G}_q^d(\vec{k}) \end{pmatrix}, \quad (23)$$

where $q = n - m \in \mathbb{Z}$. The 3×3 matrices are given by

$$\mathcal{G}_q^d(\vec{k}) = \Lambda^0 \delta_{q,0} + t_1 \Lambda_q(\vec{k}_\parallel), \quad (24)$$

$$\mathcal{G}_q^o(\vec{k}) = t_2 \Lambda_q(\vec{k}_\parallel) + t_c \Lambda_q^z(k_z). \quad (25)$$

The Λ_q matrices are given by

$$\Lambda_q^z(k_z) = \frac{1}{2} \left(\tilde{\Lambda}_q^z(k_z) + \tilde{\Lambda}_{-q}^{z*}(k_z) \right) \mathbf{I}_{3 \times 3}, \quad (26)$$

$$\Lambda_q(\vec{k}_\parallel) = \frac{1}{2} \left(\tilde{\Lambda}_q(\vec{k}_\parallel) + \tilde{\Lambda}_{-q}^*(\vec{k}_\parallel) \right), \quad (27)$$

where

$$\tilde{\Lambda}_q^z(k_z) = \mathcal{J}_q(\mathcal{E}_z) e^{ik_z} e^{iq\phi}, \quad (28)$$

$$\tilde{\Lambda}_q(\vec{k}_\parallel) = \begin{pmatrix} 0 & f_{q,AB} & f_{q,CA} \\ f_{q,AB}^* & 0 & f_{q,BC} \\ f_{q,CA}^* & f_{q,BC}^* & 0 \end{pmatrix}, \quad (29)$$

with

$$f_{q,AB} = \mathcal{J}_q(\sqrt{3}\mathcal{E}_y/2) e^{ik_1^\parallel}, \quad (30)$$

$$f_{q,BC} = \delta_{q,0} e^{ik_2^\parallel}, \quad (31)$$

$$f_{q,CA} = \mathcal{J}_q(\sqrt{3}\mathcal{E}_y/2) e^{ik_3^\parallel}. \quad (32)$$

Here $\mathcal{J}_q(x)$ is the Bessel function of order q . The intensity of light in the magnonic Floquet formalism is characterized by the dimensionless quantity \mathcal{E}_i given by Eq. (2).

IV. HIGH-FREQUENCY LIMIT

We will study the off-resonant limit $\hbar\omega \gg J, D_z, J_c$, when the system can be described by an effective time-

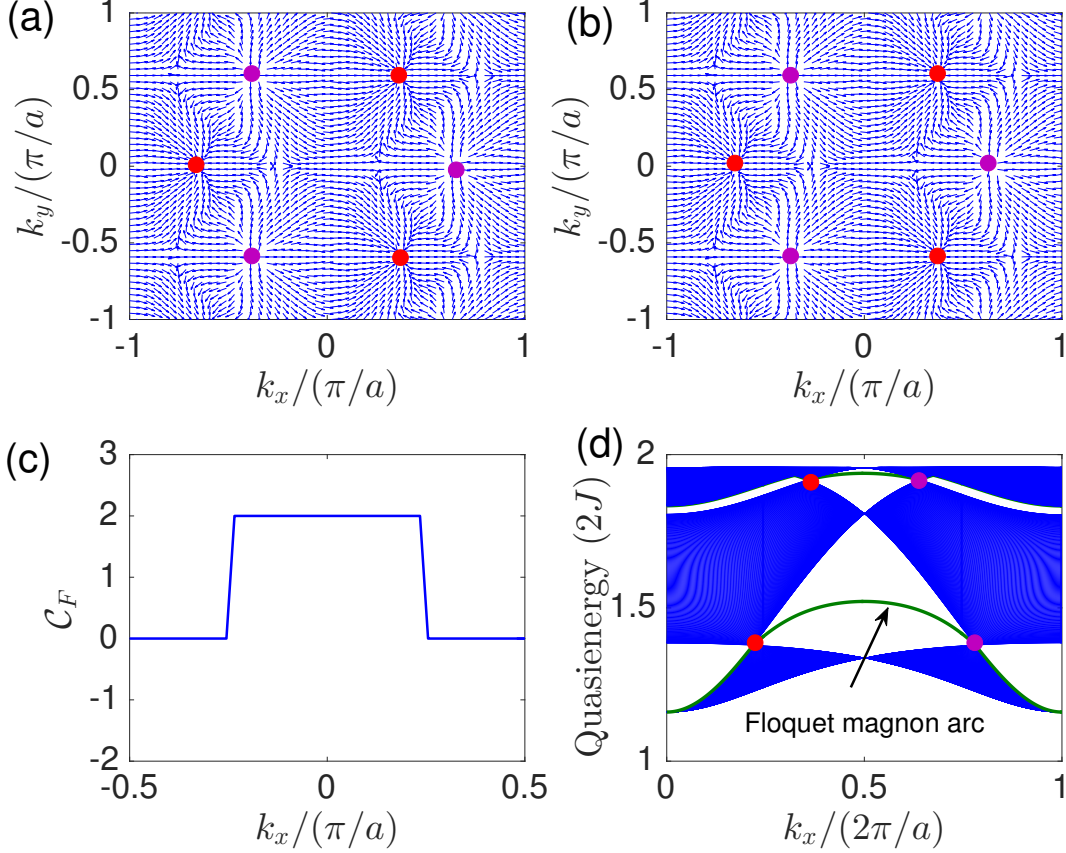


FIG. 4. Color online. Top panel. Photoinduced Berry curvature monopoles of the acoustic topological Floquet Weyl magnon nodes on the $k_z = \pi$ plane for (a) linearly-polarized light $\phi = 0$ and (b) circularly-polarized light $\phi = \pi/2$. Bottom panel. (c) The Floquet Chern number of the acoustic magnon quasienergy band as function of k_x for circularly-polarized light $\phi = \pi/2$. (d) (010)-surface magnon quasienergy band structure along a line connecting a pair of Floquet Weyl magnon nodes with opposite chirality for circularly-polarized light $\phi = \pi/2$ at $k_z = \pi$. The parameters are $S = 1/2$, $D_z/J = 0.2$, $J_c/J = 0.5$, $\mathcal{E}_y = \mathcal{E}_z = 1$ and $\omega/J = 10$.

independent Hamiltonian [8, 12], given by

$$\mathcal{H}_{eff}(\vec{k}) = \mathcal{H}_0(\vec{k}) - \frac{1}{\hbar\omega} [\mathcal{H}_{-1}(\vec{k}), \mathcal{H}_1(\vec{k})]. \quad (33)$$

As we mentioned above, in terms of the original spin operators, the first term is the original static spin model with renormalized interactions, whereas the second term breaks time-reversal symmetry by inducing additional spin interactions. The effective Floquet bosonic BdG Hamiltonian $\mathcal{H}_{eff}(\vec{k})$ can be diagonalized numerically using the generalized Bogoliubov transformation. To do this, we make a linear transformation $\psi(\vec{k}) = \mathcal{P}(\vec{k})\mathcal{M}(\vec{k})$, where $\mathcal{P}(\vec{k})$ is a $2N \times 2N$ paraunitary matrix defined as

$$\mathcal{P}(\vec{k}) = \begin{pmatrix} u_{\vec{k}} & -v_{\vec{k}}^* \\ -v_{\vec{k}} & u_{\vec{k}}^* \end{pmatrix}, \quad (34)$$

where $u_{\vec{k}}$ and $v_{\vec{k}}$ are $N \times N$ matrices that satisfy the relation

$$|u_{\vec{k}}|^2 - |v_{\vec{k}}|^2 = \mathbb{I}_{N \times N}. \quad (35)$$

The quasiparticle operators are given by $\mathcal{M}^\dagger(\vec{k}) = (m^\dagger(\vec{k}), m(-\vec{k}))$ with $m^\dagger(\vec{k}) = (b_{kA}^\dagger, b_{kB}^\dagger, b_{kC}^\dagger)$. The paraunitary operator $\mathcal{P}(\vec{k})$ satisfies the relations

$$\mathcal{P}^\dagger(\vec{k})\mathcal{H}_{eff}(\vec{k})\mathcal{P}(\vec{k}) = \mathcal{E}(\vec{k}), \quad \mathcal{P}^\dagger(\vec{k})\tau_3\mathcal{P}(\vec{k}) = \tau_3, \quad (36)$$

where

$$\mathcal{E}(\vec{k}) = \begin{pmatrix} \epsilon_n(\vec{k}) & 0 \\ 0 & \epsilon_n(-\vec{k}) \end{pmatrix}, \quad \tau_3 = \begin{pmatrix} \mathbb{I}_{N \times N} & 0 \\ 0 & -\mathbb{I}_{N \times N} \end{pmatrix}. \quad (37)$$

Using Eq. (36), we see that the Hamiltonian to be diagonalized is $\mathcal{H}_{eff}^B(\vec{k}) = \tau_3\mathcal{H}_{eff}(\vec{k})$, whose eigenvalues are given by $\tau_3\mathcal{E}(\vec{k})$ and the columns of $\mathcal{P}(\vec{k})$ are the corresponding eigenvectors.

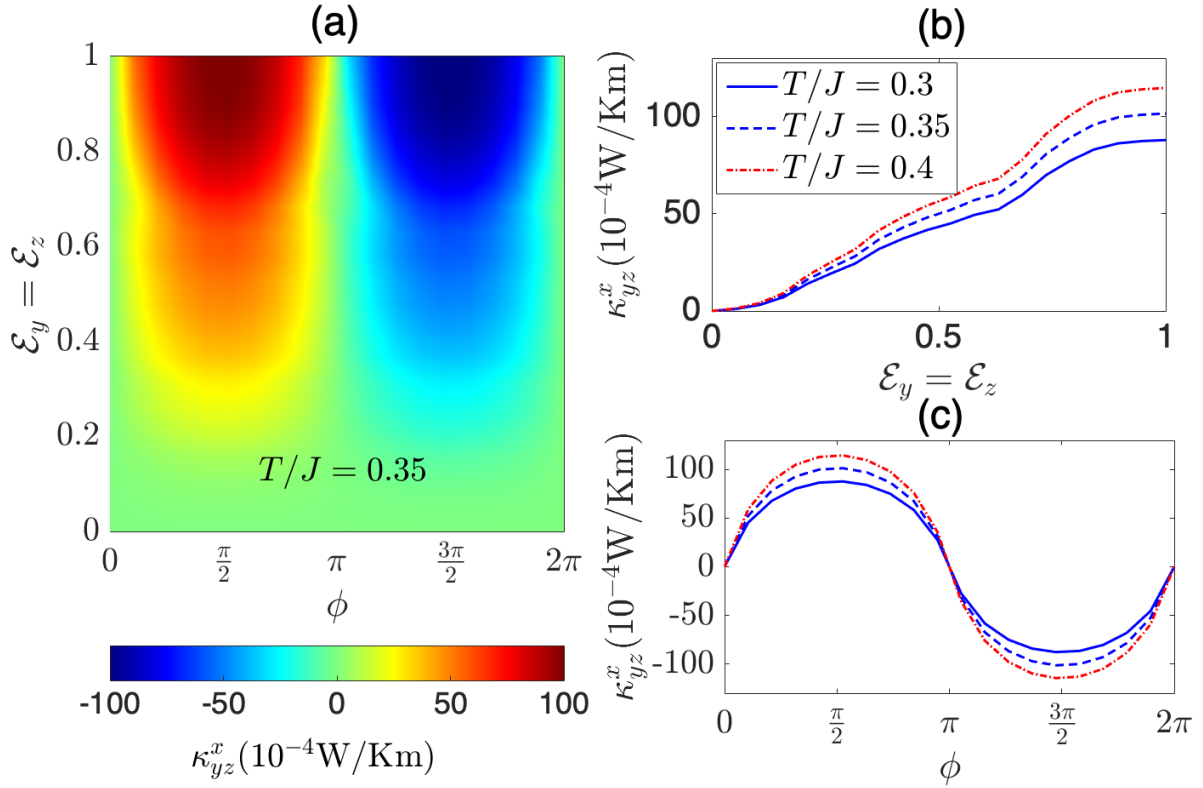


FIG. 5. Color online. Photoinduced Floquet thermal Hall conductivity κ_{yz}^x in the (a) $\phi - \mathcal{E}$ plane for $T/J = 0.35$, (b) as a function of light intensity $\mathcal{E}_y = \mathcal{E}_z$ for $\phi = \pi/2$, and (c) as a function of phase difference ϕ for $\mathcal{E}_y = \mathcal{E}_z = 1$. The other parameters are $S = 1/2$, $D_z/J = 0.2$, $J_c/J = 0.5$ and $\omega/J = 10$.

A. Photoinduced Floquet Weyl magnon bands

In Fig. (3)(a) we have shown the undriven (*i.e.* $\mathcal{E}_y = \mathcal{E}_z = 0$) magnon bands of 3D noncollinear spin structure in the kagome antiferromagnets along the BZ paths depicted in Fig. (2)(c). The system possesses nodal line magnon at the A point and along the lines Γ - K and K - H . There also exists a triply-degenerate nodal magnon points along the line A - Γ where three magnon branches linearly cross each other. The details of these magnon nodal line phases have been previously discussed [32], and they are protected by the crystal symmetry of the kagome lattice as discussed in Sec. (II B). As the periodic drive is turned on, we expect the symmetry protection of the nodal line magnons to be broken by the light intensity.

Indeed, in Fig. (3)(b) we can see that the nodal line magnons at the A point is split into six Floquet Weyl magnon (Floquet Weyl magnon) nodes (only two are independent) located along the k_x direction at $\vec{k}_{Q_1} = [\pm \cos^{-1}(Q_1), 0, \pi]$ and $\vec{k}_{Q_2} = [\pm \cos^{-1}(Q_2), \pm\pi/3, \pi]$. Due to the complexity of this model we could not find an explicit analytical form for Q_1 and Q_2 . There are 3 pairs of Floquet Weyl magnon nodes with opposite chiralities on the $k_z = \pi$ plane as indicated in Fig. (2)(d).

The triply-degenerate nodal magnon points along the A - Γ line is also split into two Floquet Weyl magnon nodes along the k_z direction. In contrast to 2D systems, we find that both linearly-polarized lights ($\phi = 0$ and $\phi = \pi$) and circularly-polarized lights ($\phi = \pi/2$) break time-reversal symmetry and induce Floquet Weyl magnon nodes in the 3D system. The reason is because the y and z directions are not symmetric in the present system. However, as we will show in the subsequent section, the Floquet magnon thermal transports for circularly-polarized light is topologically nontrivial, whereas those for linearly-polarized light is topologically trivial. We also note that the incident light breaks $U(1)$ spin rotation and lifts the Goldstone modes at the Γ point as shown in Fig. (3)(b).

B. Photoinduced Berry curvature

Usually, the analysis of the band structure is not sufficient to proof that a non-degenerate linear band crossing in 3D system forms topological Weyl nodes. The existence of topological Weyl nodes can be reinforced by computing the Berry curvature of the linear band crossing. Topological Weyl nodes act as the source and sink of the Berry curvature. This implies that a single Weyl node can be considered as the monopole of the Berry curva-

ture. Using the paraunitary operator, we can define the photoinduced Floquet Berry curvature as

$$\Omega_{\alpha\beta,n}^{\gamma}(\vec{k}) = -2\text{Im} \sum_{m \neq n} \frac{[\langle \mathcal{P}_{\vec{k}n}^{\dagger} | \hat{v}_{\alpha} | \mathcal{P}_{\vec{k}m}^{\dagger} \rangle \langle \mathcal{P}_{\vec{k}m}^{\dagger} | \hat{v}_{\beta} | \mathcal{P}_{\vec{k}n}^{\dagger} \rangle]}{[\epsilon_m(\vec{k}) - \epsilon_n(\vec{k})]^2}, \quad (38)$$

where $\hat{v}_{\alpha} = \partial \mathcal{H}_{\text{eff}}^B(\vec{k}) / \partial k_{\alpha}$ defines the photoinduced velocity operators with $\alpha, \beta, \gamma = x, y, z$ and n labels the Floquet magnon branches. The photoinduced Berry curvature can be considered as a 3-pseudo-vector pointing along the γ directions perpendicular to both the α and β directions. It diverges at the photoinduced Floquet Weyl magnon nodes as can be seen from the denominator of Eq. (38).

In Fig. (4)(a) and Fig. (4)(b) we have shown the photoinduced Berry curvature $\Omega_{xy,1}^z(\vec{k})$ in the $k_z = \pi$ plane for the acoustic Floquet magnon band. Indeed, we can see that the topological Floquet Weyl magnon nodes at \vec{k}_{Q_1} and \vec{k}_{Q_2} are the monopoles and anti-monopoles of the Floquet Berry curvature for both linearly- and circularly-polarized lights.

Along the line $H-A$ there are two independent Floquet Weyl points located at $\pm k_x^c$. For the 2D planes for fixed $k_x \neq \pm k_x^c$ the system is gapped and can be considered as a Floquet Chern insulator. Hence, we can define the Floquet Chern number for fixed k_x as

$$\mathcal{C}_n^F(k_x) = \frac{1}{2\pi} \int_{BZ} dk_y dk_z \Omega_{yz,n}^x(k_x, k_y, k_z). \quad (39)$$

In Fig. (4)(c) we have shown the plot of the Floquet Chern number of the acoustic magnon quasienergy branch as a function of k_x for circularly-polarized light $\phi = \pi/2$. We can see that $\mathcal{C}^F = 0$ for planes with $k_x < -k_x^c$ or $k_x > k_x^c$, while $\mathcal{C}^F = 2$ for planes with $-k_x^c < k_x < k_x^c$. This implies that the magnon quasienergy band crossing between the planes with $\mathcal{C}^F = 2$ and $\mathcal{C}^F = 0$ are indeed Floquet Weyl points.

One of the hallmarks of equilibrium Weyl semimetals is the formation of Fermi arcs which connect the surface projection of the Weyl points in the BZ. Indeed, as shown in Fig. (4)(d) we can see that the (010)-projected Floquet Weyl magnon points with opposite chirality are connected by Floquet magnon arc surface states. These hallmark properties of equilibrium Weyl semimetals confirm that the non-degenerate magnon quasienergy linear band crossings in the present system are indeed topological Floquet Weyl magnon points.

C. Photoinduced thermal Hall effect

Another hallmark of equilibrium Weyl semimetals is the appearance of the anomalous Hall effect. For magnon quasiparticles with no charge, the corresponding transport property is the anomalous thermal Hall effect in

the presence of a temperature gradient [52–56]. In the nonequilibrium system, it is customary to assume the limit in which the occupation function of the quasiparticle excitations is close to equilibrium. Therefore, we can write the photoinduced thermal Hall conductivity in the usual form [54]

$$\kappa_{\alpha\beta}^{\gamma} = -k_B T \int_{BZ} \frac{d\vec{k}}{(2\pi)^3} \sum_{n=1}^N c_2(f_n^B) \Omega_{\alpha\beta,n}^{\gamma}(\vec{k}), \quad (40)$$

where $f_n^B = (e^{\epsilon_n(\vec{k})/k_B T} - 1)^{-1}$ is the Bose occupation function close to equilibrium, k_B the Boltzmann constant which we will set to unity, T is the temperature and $c_2(x) = (1+x)(\ln \frac{1+x}{x})^2 - (\ln x)^2 - 2\text{Li}_2(-x)$ weight function with $\text{Li}_2(x)$ being the dilogarithm.

In Fig. (5) we have shown the trends of the photoinduced thermal Hall conductivity κ_{yz}^x in the $\phi - \mathcal{E}$ plane at $T/J = 0.35$ (a), as a function of $\mathcal{E}_y = \mathcal{E}_z$ (b), and as a function of ϕ (c) for $T/J = 0.3, 0.35, 0.4$. In Fig. (5)(b), we can see that κ_{yz}^x vanishes in the limit of undriven system $\mathcal{E}_y = \mathcal{E}_z = 0$. This is due to the presence of time-reversal symmetry in the undriven in-plane 120° spin structure, which leads to zero Berry curvature. Although the photoinduced Berry curvature of the Floquet Weyl points is nonzero for linearly-polarized light $\phi = 0$ or $\phi = \pi$, we can see in Fig. (5)(c) that κ_{yz}^x vanishes at $\phi = 0$ and $\phi = \pi$. Therefore, the Floquet magnon thermal transports for linearly-polarized light is topologically trivial.

D. Photoinduced chiral spin structure

We would like to address the nature of the photoinduced spin structure that gives rise to the topological magnon properties in this system. It is evident that in the periodically driven 3D non-collinear kagome antiferromagnets, there is no photoinduced noncoplanar spin structure with nonzero scalar spin chirality. This is because light propagates parallel to the in-plane 120° spin structure (i.e. along the in-plane x direction). Therefore, the topological Floquet Weyl magnons can only originate from a photoinduced canted in-plane 120° chiral spin structure with no finite scalar spin chirality, but time-reversal symmetry is broken through the second term in Eq. (33). We note that the intrinsic equilibrium form of this canted in-plane 120° chiral spin structure was observed recently in the electronic stacked kagome noncollinear antiferromagnets $\text{Mn}_3\text{Sn}/\text{Ge}$ [48–51], which are also antiferromagnetic Weyl semimetals. Therefore, the mechanism that gives rise to the topological Floquet Weyl magnons is different from that of equilibrium Weyl magnon nodes induced by noncoplanar chiral spin structure [32].

V. CONCLUSION AND OUTLOOK

We have shown that laser-irradiated noncollinear stacked kagome antiferromagnets with a symmetry-protected three-dimensional (3D) in-plane 120° spin structure can be tuned to a topological Floquet Weyl magnon semimetal. They arise when the incident light propagates parallel to the in-plane 120° spin structure. We showed that the topological Floquet Weyl magnon semimetal in the periodically driven noncollinear stacked kagome antiferromagnets originate from a photoinduced canted 3D in-plane 120° chiral spin structure, whose intrinsic equilibrium form was recently observed in the electronic noncollinear stacked kagome antiferromagnets $\text{Mn}_3\text{Sn}/\text{Ge}$ [48–51]. We also studied the experimental measurable photoinduced thermal Hall effect due to the Berry curvature of the Floquet Weyl magnon nodes. We believe that the current results are within experimental reach and can be accessible with the current terahertz frequency using ultrafast terahertz spectroscopy. The current results also pave the way for manipulating the intrinsic properties of geometrically frustrated kagome antiferromagnets. It is believed that topological antiferromagnets have potential technological applications in spintronics [57, 58], because they have zero net spin magnetization which makes their magnetism externally invisible and insensitive to external magnetic fields.

Most studies in Floquet topological systems customarily assume that the quasienergy levels of the Floquet Hamiltonian are close to the equilibrium system [1–5]. Therefore, the properties of equilibrium topological systems can be applied to Floquet topological systems. However, Floquet topological systems are inherently out of equilibrium and thus the question about the non-equilibrium distribution function of the quasiparticles becomes important. In the present case, the distribution function of magnon enters observable quantities such as the thermal Hall effect. In the non-equilibrium system, the distribution function of magnon will depend on how the periodic drive is switched on [59, 60]. Therefore, the topological properties of the non-equilibrium system will be completely different from that of equilibrium system. To study the non-equilibrium system, one can consider an open system in which magnon couples to external reservoir of phonons. Alternatively, one can consider the dynamics of the system in a quantum quench when the periodic drive is suddenly switched on. However, a complete analysis of this study is beyond the purview of this paper. We plan to address this problem in future work as we continue to develop the study of Floquet topological magnons.

ACKNOWLEDGEMENTS

Research at Perimeter Institute is supported by the Government of Canada through Industry Canada and by the Province of Ontario through the Ministry of Research

and Innovation.

APPENDIX A. PHOTOINDUCED 2D TOPOLOGICAL MAGNON INSULATOR

A. Time-independent spin model

In this appendix, we will study phases *I* and *II* in Fig. (1). In these phases the interlayer coupling can be neglected and thus the Hamiltonian reduces to a strictly 2D system. We will consider the 2D strained Heisenberg antiferromagnetic spin Hamiltonian given by

$$\mathcal{H} = \sum_{\langle ij \rangle} J_{ij} \vec{S}_i \cdot \vec{S}_j + \sum_{\langle ij \rangle} \vec{D}_{ij} \cdot \vec{S}_i \times \vec{S}_j, \quad (41)$$

where $J_{ij} = J$ on the diagonal bonds and $J_{ij} = J'$ on the horizontal bonds with $\delta \neq 1$ being the strain or lattice distortion. The DM interaction is still out-of-plane, *i.e.* $\vec{D}_{ij} = -D_z \hat{z}$. For $D_z = 0$ the classical ground state yields the strained induced canting angle

$$\varphi = \arccos\left(-\frac{1}{2}\delta\right). \quad (42)$$

Note that $\varphi \neq 120^\circ$ for $\delta \neq 1$. The limiting case $\delta \rightarrow 0$ maps to a bipartite square-lattice with collinear magnetic order, whereas $\delta \rightarrow \infty$ maps to a decoupled antiferromagnetic spin chain. The canted coplanar spin structure is stabilized for $\delta > 1/2$, but it also has an extensive degeneracy as in the case of ideal kagome Heisenberg antiferromagnet at $\delta = 1$. However, the extensive degeneracy is lifted by a finite DM interaction $D_z \neq 0$ and thus a unique ground state is selected.

B. Time-dependent bosonic model

We will study the magnon excitations of the non-collinear system for $\delta > 1/2$ in the presence of an oscillating electric field propagating along the z -direction perpendicular to the x - y plane, which is given by

$$\vec{\Xi}(\tau) = [E_y \sin \omega\tau, E_x \sin(\omega\tau + \phi), 0], \quad (43)$$

where $\vec{\Xi}(\tau) = \vec{E}(\tau) \times \hat{z}$.

Following the same procedure outlined above, we find that the Fourier components of the Floquet bosonic BdG Hamiltonian are given by

$$\mathcal{H}_q(\vec{k}) = 2JS \begin{pmatrix} \mathcal{G}_q^d(\vec{k}) & \mathcal{G}_q^o(\vec{k}) \\ \mathcal{G}_q^o(\vec{k}) & \mathcal{G}_q^d(\vec{k}) \end{pmatrix}. \quad (44)$$

The 3×3 matrices in this case have a different form given by

$$\mathcal{G}_q^d(\vec{k}) = \Lambda^0 \delta_{q,0} + \Lambda_q^{(1)}(\vec{k}_\parallel), \quad \mathcal{G}_q^o(\vec{k}) = \Lambda_q^{(2)}(\vec{k}_\parallel), \quad (45)$$

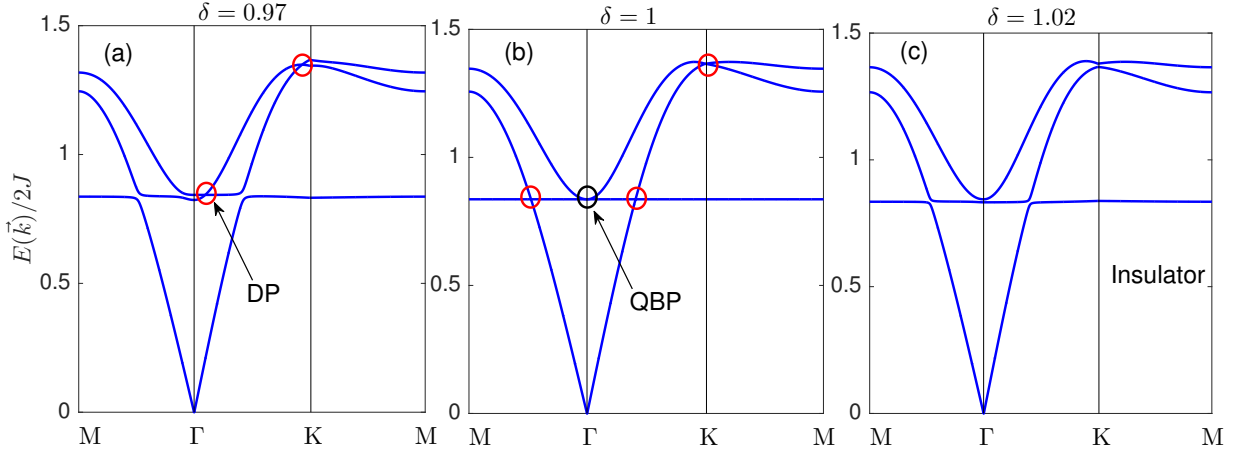


FIG. 6. Color online. Strained-induced magnon phase transition of undriven 2D kagome antiferromagnets for $D_z/J = 0.2$ and $\mathcal{E}_x = \mathcal{E}_y = 0$. (a) $\delta = 0.97$ with Dirac point (DP) along the Γ -K line. (b) $\delta = 1$ isotropic limit with quadratic band crossing point (QBP) at Γ . (c) $\delta = 1.02$ with no magnon band crossing point.

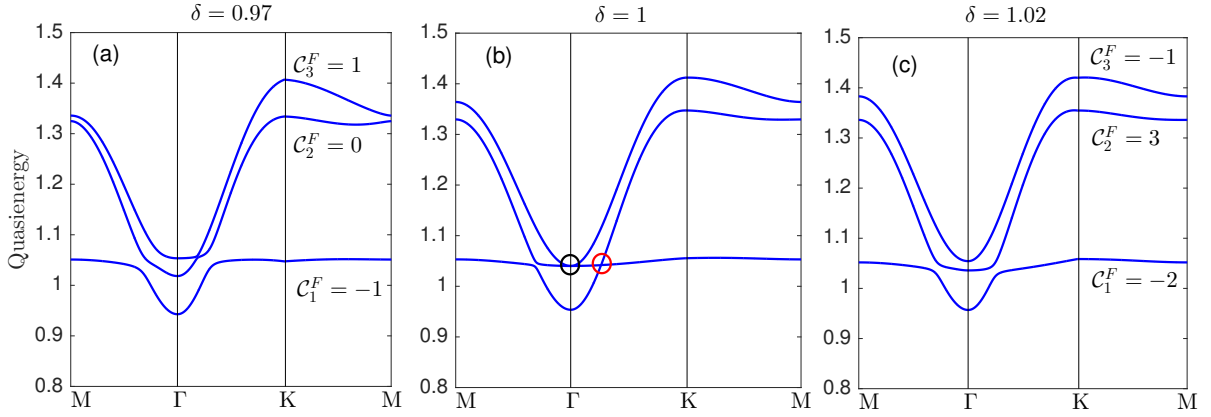


FIG. 7. Color online. Floquet strained-induced topological magnon phase transition of periodically driven 2D kagome antiferromagnets for $D_z/J = 0.2$ and $\mathcal{E}_x = \mathcal{E}_y = 1$ and $\phi = \pi/2$. (a) $\delta = 0.97$ with Floquet magnon Chern numbers $\mathcal{C}^F = (-1, 0, -1)$. (b) $\delta = 1$ phase transition point. (c) $\delta = 1.02$ with Floquet magnon Chern numbers $\mathcal{C}^F = (-2, 3, -1)$.

where

$$\Lambda^0 = \text{diag}(\xi_{AA}, \xi_{BB}, \xi_{CC}), \quad (46)$$

with the parameter given by

$$\xi_{AA} = -2(\cos \varphi - D_J \sin \varphi), \quad (47)$$

$$\xi_{BB} = \xi_{CC} = -\delta(\cos 2\varphi + D_J \sin 2\varphi) + \xi_{AA}/2. \quad (48)$$

We have used the notation $D_J = D_z/J$ for brevity. The $\Lambda_q^{(i)}$ matrices are given by

$$\Lambda_q^{(i)}(\vec{k}^{\parallel}) = \frac{1}{2} \left(\tilde{\Lambda}_q^{(i)}(\vec{k}^{\parallel}) + [\tilde{\Lambda}_{-q}^{(i)}]^*(\vec{k}^{\parallel}) \right), \quad (49)$$

where

$$\tilde{\Lambda}_q^{(i)}(\vec{k}^{\parallel}) = \begin{pmatrix} 0 & a_i f_{q,AB} & a_i f_{q,CA} \\ a_i f_{q,AB}^* & 0 & \tilde{a}_i f_{q,BC} \\ a_i f_{q,CA}^* & \tilde{a}_i f_{q,BC}^* & 0 \end{pmatrix}. \quad (50)$$

The constant a_i factors are given by

$$a_1 = \frac{1}{2}(1 + \cos \varphi - D_J \sin \varphi), \quad (51)$$

$$\tilde{a}_1 = \delta(\cos 2\varphi + \sin^2 \varphi + D_J \sin \varphi \cos \varphi), \quad (52)$$

$$a_2 = \frac{1}{2}(1 - \cos \varphi + D_J \sin \varphi), \quad (53)$$

$$\tilde{a}_2 = \delta \sin^2 \varphi - D_J \sin \varphi \cos \varphi. \quad (54)$$

The f functions are given by

$$f_{q,AB} = \mathcal{J}_q(\mathcal{E}_+) e^{iq\Psi_+} e^{ik_1^{\parallel}}, \quad (55)$$

$$f_{q,BC} = \mathcal{J}_q(\mathcal{E}_x) e^{ik_2^{\parallel}}, \quad (56)$$

$$f_{q,CA} = \mathcal{J}_q(\mathcal{E}_-) e^{-iq\Psi_-} e^{ik_3^{\parallel}}, \quad (57)$$

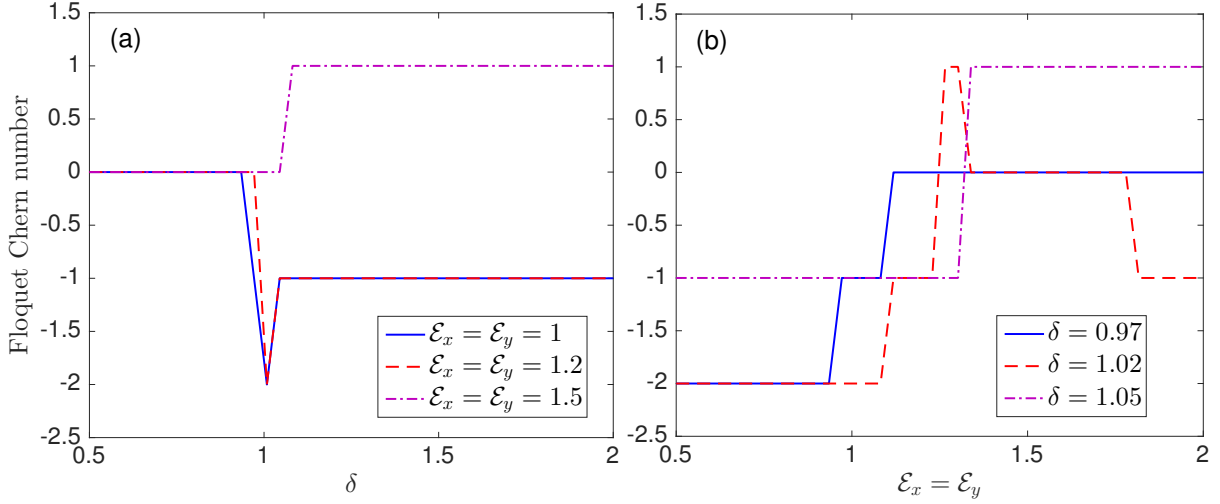


FIG. 8. Color online. Plot of Floquet Chern number of the lowest quasienergy magnon band as a function of (a) δ and (b) $\mathcal{E}_x = \mathcal{E}_y$, for $\phi = \pi/2$.

where $\mathcal{J}_n(x)$ is the Bessel function of order n .

$$\mathcal{E}_{\pm} = \frac{1}{2} \sqrt{3\mathcal{E}_x^2 + \mathcal{E}_y^2 \pm 2\sqrt{3}\mathcal{E}_x\mathcal{E}_y \cos(\phi)}, \quad (58)$$

$$\Psi_{\pm} = \arctan\left(\frac{\sqrt{3}\mathcal{E}_x \sin(\phi)}{\mathcal{E}_y \pm \sqrt{3}\mathcal{E}_x \cos(\phi)}\right). \quad (59)$$

C. Photoinduced Floquet topological magnon phase transition

We will now study the topological magnon phase transition associated with the 2D strained kagome antiferromagnets in the presence of circularly-polarized electric field. Let us first consider the undriven system. In Fig. 6 we have shown the magnon bands of the undriven 2D strained kagome antiferromagnets for varying δ . We can see that the Dirac magnon “semimetal” in the regime $0 < \delta \leq 1$ can be turned to a trivial insulator for $\delta > 1$. As shown Fig. 7, we can see that

circularly-polarized electric field induces a Floquet topological magnon phase transition across the topological phase boundary at the isotropic point $\delta = 1$. To investigate the complete photoinduced Floquet topological magnon phase transition, we define the Floquet Chern number of quasienergy magnon bands as

$$\mathcal{C}_n^F = \frac{1}{2\pi} \int_{BZ} d^2k \Omega_{xy,n}^z(\vec{k}). \quad (60)$$

In Fig. 8 we have shown the evolution of the lowest Floquet magnon Chern number as a function of δ for varying amplitudes (a) and as a function of $\mathcal{E}_x = \mathcal{E}_y$ for varying δ (b). In both cases we have considered circularly-polarized electric field $\phi = \pi/2$. We note that the Floquet Chern number vanishes for linearly polarized light in the 2D systems. We can see that the lowest Floquet magnon Chern number varies in the range $\mathcal{C}_1^F = (-2, -1, 0, 1)$ which indicates a photoinduced Floquet topological magnon phase transition in the driven 2D strained kagome antiferromagnets.

-
- [1] T. Oka, and H. Aoki, *Phys. Rev. B* **79**, 081406 (2009).
 - [2] J. -I. Inoue and A. Tanaka, *Phys. Rev. Lett.* **105**, 017401 (2010).
 - [3] N. Lindner, G. Refael, and V. Gaslitiski, *Nat. Phys.* **7**, 490 (2011).
 - [4] H. L. Calvo, H. M. Pastawski, S. Roche, and L. E. F. Foa Torres, *Appl. Phys. Lett.* **98**, 232103 (2011).
 - [5] T. Kitagawa, T. Oka, A. Brataas, L. Fu, and E. Demler, *Phys. Rev. B* **84**, 235108 (2011).
 - [6] Y. H. Wang, H. Steinberg, P. Jarillo-Herrero, N. Gedik, *Science* **342**, 453 (2013).
 - [7] R. Wang et al. *Europhys. Lett.* **105**, 17004 (2014).
 - [8] A. G. Grushin, Á. Gómez-León, and T. Neupert, *Phys. Rev. Lett.* **112**, 156801 (2014).
 - [9] G. Jotzu, M. Messer, R. Desbuquois, Ma. Lebrat, Th. Uehlinger, D. Greif, and T. Esslinger, *Nature* **515**, 237 (2014).
 - [10] N. Fläschner, B. S. Rem, M. Tarnowski, D. Vogel, D.-S. Lühmann, K. Sengstock, C. Weitenberg, *Science* **352**, 1091 (2016).
 - [11] S. Ebihara, K. Fukushima, and T. Oka, *Phys. Rev. B* **93**, 155107 (2016).
 - [12] Z. Yan and Z. Wang, *Phys. Rev. Lett.* **117**, 087402 (2016).

- [13] X.-X. Zhang, T. Tzen Ong, and N. Nagaosa, *Phys. Rev. B* **94**, 235137 (2016).
- [14] N. Goldman and J. Dalibard, *Phys. Rev. X* **4**, 031027 (2014).
- [15] M. Bukov, L. D'Alessio, and A. Polkovnikov, *Advances in Physics* **64**, 139, (2015).
- [16] R. Roy and F. Harper, *Phys. Rev. B* **96**, 155118 (2017).
- [17] Z. Yan and Z. Wang, *Phys. Rev. B* **96**, 041206(R) (2017).
- [18] H. Hübener, M. A. Sentef, U. de Giovannini, A. F. Kemper, and A. Rubio, *Nat. Commun.* **8**, 13940 (2017).
- [19] L. Du, X. Zhou, and G. A. Fiete, *Phys. Rev. B* **95**, 035136 (2017).
- [20] Y. Wang, Y. Liu, and B. Wang, *Sci. Rep.* **7**, 41644 (2017).
- [21] K. Takasan, M. Nakagawa, and N. Kawakami, *arXiv:1706.06114* (2017).
- [22] M. Claassen, H. -C. Jiang, B. Moritz, and T. P. Devereaux, *Nat. Commun.* **8**, 1192 (2017).
- [23] E. A. Stepanov, C. Dutreix, and M. I. Katsnelson, *Phys. Rev. Lett.* **118**, 157201 (2017).
- [24] S. A. Owerre, *J. Phys. Commun.* **1**, 021002 (2017); Corrigendum, *J. Phys. Commun.* **2** (2018) 109501.
- [25] Y. Aharonov and A. Casher, *Phys. Rev. Lett.* **53**, 319 (1984).
- [26] S. A. Owerre, *Sci. Rep.* **8**, 10098 (2018).
- [27] S. A. Owerre, *Annals of Physics* **399** 93 (2018).
- [28] S. A. Owerre, *Sci. Rep.* **8**, 4431 (2018).
- [29] J. Walowski and M. Münzenberg, *J. Appl. Phys.* **120**, 140901 (2016).
- [30] F.-Y. Li, Y.-D. Li, Y.B. Kim, L. Balents, Y. Yu, and G. Chen. *Nat. Commun.* **7**, 12691 (2016).
- [31] S.-K. Jian and W. Nie. *Phys. Rev. B*, **97**, 115162 (2018).
- [32] S. A. Owerre, *Phys. Rev. B* **97**, 094412 (2018).
- [33] S. A. Owerre, *Can. J. Phys.* **96**, 1216 (2018).
- [34] S. A. Owerre, *Phys. Rev. B* **95**, 014422 (2017).
- [35] P. Laurell and G. A. Fiete, *Phys. Rev. B* **98**, 094419 (2018).
- [36] A. Mook, J. Henk, and I. Mertig, *Phys. Rev. B* **99**, 014427 (2019).
- [37] Y. Lu, X. Guo, V. Koval, and C. Jia, *Phys. Rev. B* **99**, 054409 (2019).
- [38] I. Dzyaloshinsky, *J. Phys. Chem. Solids* **4**, 241 (1958).
- [39] T. Moriya, *Phys. Rev.* **120**, 91 (1960).
- [40] K. Matan, D. Grohol, D. G. Nocera, T. Yildirim, A. B. Harris, S. H. Lee, S. E. Nagler, and Y. S. Lee, *Phys. Rev. Lett.* **96**, 247201 (2006).
- [41] T. -H. Han, J. S. Helton, S. Chu, D. G. Nocera, J. A. Rodriguez-Rivera, C. Broholm, and Y. S. Lee, *Nature* **492**, 406 (2012).
- [42] R. Okuma, T. Yajima, D. Nishio-Hamane, T. Okubo, and Z. Hiroi, *Phys. Rev. B* **95**, 094427 (2017).
- [43] M. Elhajal, B. Canals, and C. Lacroix, *Phys. Rev. B* **66**, 014422 (2002).
- [44] D. Gosálbez-Martínez, I. Souza, and D. Vanderbilt, *Phys. Rev. B* **92**, 085138 (2015).
- [45] M.- T. Suzuki, T. Koretsune, M. Ochi, and R. Arita, *Phys. Rev. B* **95**, 094406 (2017).
- [46] K. Nakata, J. Klinovaja, and D. Loss, *Phys. Rev. B*, **95**, 125429 (2017).
- [47] Y. Su and X. R. Wang, *Phys. Rev. B* **96**, 104437 (2017).
- [48] S. Nakatsuji, N. Kiyohara, and T. Higo, *Nature* **527**, 212 (2015).
- [49] N. Kiyohara, T. Tomita, and S. Nakatsuji, *Phys. Rev. Applied* **5**, 064009 (2016).
- [50] A. K. Nayak, Julia Fischer, Yan Sun, Binghai Yan, Julie Karel, Alexander Komarek, Chandra Shekhar, Nitesh Kumar, Walter Schnelle, Juergen Kuebler, Claudia Felser, Stuart S. P. Parkin, *Sci. Adv.* **2** e1501870 (2016).
- [51] H. Yang, Yan Sun, Yang Zhang, Wu-Jun Shi, Stuart S. P. Parkin, Binghai Yan, *New J. Phys.* **19** 015008 (2017).
- [52] H. Katsura, N. Nagaosa, and P. A. Lee, *Phys. Rev. Lett.* **104**, 066403 (2010).
- [53] Y. Onose, T. Ideue, H. Katsura, Y. Shiomi, N. Nagaosa, and Y. Tokura, *Science* **329**, 297 (2010).
- [54] R. Matsumoto and S. Murakami, *Phys. Rev. Lett.* **106**, 197202 (2011). *Phys. Rev. B*, **84**, 184406 (2011).
- [55] T. Ideue, Y. Onose, H. Katsura, Y. Shiomi, S. Ishiwata, N. Nagaosa, and Y. Tokura, *Phys. Rev. B*, **85**, 134411 (2012).
- [56] M. Hirschberger, R. Chisnell, Y. S. Lee, and N. P. Ong, *Phys. Rev. Lett.* **115**, 106603 (2015).
- [57] L. Smejkal, T. Jungwirth, and J. Sinova, *Phys. Status Solidi RRL* **11**, 1700044 (2017).
- [58] A. V. Chumak, V. I. Vasyuchka, A. A. Serga, and B. Hillebrands, *Nat. Phys.* **11**, 453 (2015).
- [59] H. Deghani, T. Oka, and A. Mitra, *Phys. Rev. B* **90**, 195429 (2014).
- [60] H. Deghani, T. Oka, and A. Mitra, *Phys. Rev. B* **91**, 155422 (2015).